AIAA JOURNAL
Vol. 62, No. 10, October 2024

Numerical Investigation of Aero-Optical Distortions from High-Speed Turbulent Boundary Layers

Pedro Castillo* and Andreas Gross†
New Mexico State University, Las Cruces, New Mexico 88003
Nathan E. Miller,‡ Kyle P. Lynch,§ and Daniel R. Guildenbecher¶
Sandia National Laboratories, Albuquerque, New Mexico 87185
and
Stanislav Gordeyev**
University of Notre Dame, Notre Dame, Indiana 46556

https://doi.org/10.2514/1.J064115

Wall-modeled large-eddy simulations of turbulent boundary-layer flows over a flat plate at Mach 3.5, 7.87, and 13.64 were carried out, and the aero-optical distortions resulting from density fluctuations were investigated. The conditions for the Mach 3.5 case match those of a direct numerical simulation in the literature. The Mach 7.87 conditions are representative of the Hypersonic Wind Tunnel at Sandia National Laboratories, and the Mach 13.64 conditions match those of the Arnold Engineering Development Complex Hypervelocity Tunnel 9. The wall-modeled large-eddy simulations were validated using available experimental and DNS reference data. The normalized root-mean-square optical path difference for all three cases is in good agreement with respective data obtained from reference direct numerical simulations and experiments (within 1.53% for $M_\infty = 3.5$, 1.25% for $M_\infty = 7.87$, and 12% for $M_\infty = 13.64$, compared to numerical data). Above $M_\infty = 5.0$, the normalized path difference obtained from the simulations is above the value predicted by a semi-analytical relationship by Notre Dame University. With increasing Mach number, the bulk contribution to the total optical distortion shifts toward the boundary-layer edge. In addition, a proper orthogonal decomposition reveals that the nature of the dominant density fluctuations, which are located near the boundary-layer edge, changes from three-dimensional to two-dimensional. Understanding how the coherent structures contribute to the optical path difference may pave a way toward devising active flow control strategies geared toward a reduction of the optical path difference.

Downloaded by University of Notre Dame on January 23, 2025 | http://arc.aiaa.org | DOI: 10.2514/1.J064115

Nomenclature

c_f	=	skin-friction coefficient
H	=	shape factor, δ/θ
K_{GD}	=	Gladstone–Dale constant
M_∞	=	Mach number
n	=	index of refraction
OPD	=	optical path difference
OPL	=	optical path length
P	=	pressure
Pr	=	Prandtl number
Q	=	vortex identification criterion
R	=	gas constant
Re	=	Reynolds number
T	=	temperature
t	=	time
u, v, w	=	velocities
u_c	=	convection velocity
u_τ	=	friction velocity, $\sqrt{\tau_w/\rho_w}$
x, y, z	=	spatial coordinates
β	=	inclination angle
γ	=	ratio of specific heats
δ	=	boundary-layer thickness
θ	=	momentum thickness
Λ	=	density correlation length
μ	=	dynamic viscosity
ν	=	kinematic viscosity
ρ	=	density
τ_w	=	wall shear stress, $Re^{-1}\mu_w \partial u/\partial y\|_w$
$\overline{(\cdot)}$	=	time averaging
$\langle\cdot\rangle$	=	area averaging over an aperture

Subscripts

i	=	incompressible value
r	=	recovery factor
rms	=	root mean square
T	=	turbulent quantity
w	=	wall variables
∞	=	freestream variables

Superscripts

$'$	=	turbulent fluctuation
$+$	=	variable in wall units
$*$	=	dimensional quantity

Presented as Paper 2022-3441 at the AIAA Aviation 2022 Forum, Chicago, IL, & Virtual, June 27–July 1, 2022; received 28 February 2024; revision received 28 May 2024; accepted for publication 10 June 2024; published online 29 August 2024. Copyright © 2024 by the American Institute of Aeronautics and Astronautics, Inc. Under the copyright claimed herein, the U.S. Government has a royalty-free license to exercise all rights for Governmental purposes. All other rights are reserved by the copyright owner. All requests for copying and permission to reprint should be submitted to CCC at www.copyright.com; employ the eISSN 1533-385X to initiate your request. See also AIAA Rights and Permissions www.aiaa.org/randp.

*Graduate Research Assistant, Mechanical and Aerospace Engineering Department; pcg1996@nmsu.edu. Member AIAA (Corresponding Author).
†Associate Professor, Mechanical and Aerospace Engineering Department. Associate Fellow AIAA.
‡Senior Member of the Technical Staff, Aerosciences Department. Senior Member AIAA.
§Principal Member of the Technical Staff, Diagnostics for Extreme Environments and Hypersonics Department. Senior Member AIAA.
¶Distinguished Member of the Technical Staff, Diagnostics for Extreme Environments and Hypersonics Department; currently Associate Professor, School of Mechanical Engineering, Purdue University. Associate Fellow AIAA.
**Associate Professor, Aerospace and Mechanical Engineering Department. Associate Fellow AIAA.

I. Introduction

COMPRESSIBILITY and wall-cooling effects for boundary-layer flows become more pronounced at higher Mach numbers [1]. The boundary layers over vehicles are often by nature turbulent or

Downloaded by University of Notre Dame on January 23, 2025 | http://arc.aiaa.org | DOI: 10.2514/1.J064115

can also be tripped to avoid uncertainties related to transition (e.g., heat transfer, sudden center of pressure shifts, and ill-defined engine inlet conditions). At high Mach numbers and for strongly cooled walls, the wall-normal temperature gradients can be substantial. The turbulent mixing of hot and cold air as well as strong shock waves cause large density fluctuations. Through the Gladstone–Dale relation, the density fluctuations translate to index-of-refraction fluctuations, which distort optical light that passes through the boundary layer [2]. At high Mach numbers (e.g., $M > 5$), the turbulent boundary layer can radiate strong acoustic noise [3], and the associated freestream density fluctuations can cause additional optical aberrations. The optical distortions compromise the performance of optical sensors, communication systems (e.g., laser), and directed-energy applications [4,5]. Therefore, the prediction of the magnitude of the aero-optical distortions is of great interest to the designers of high-speed flight vehicles.

The optical aberrations caused by high-speed turbulent boundary-layer flows have been investigated since the early 1950s, starting with the pioneering experimental work by Liepmann [6]. Truman carried out direct numerical simulations (DNSs) of incompressible turbulent shear flows [7,8] and found that the large energy-bearing structures are mainly responsible for the optical path differences (OPDs). According to Tromeur et al. [9], the optical distortions depend strongly on the beam direction. Follow-up turbulent boundary-layer experiments by Cress et al. [10] suggested that the beam experienced larger distortions when it was tilted toward the downstream direction. Aero-OPDs of collimated optical wavefronts transmitted through compressible turbulent boundary-layer flows were then investigated experimentally by, e.g., Gordeyev et al. [11–13] and Lynch et al. [14], and numerically by, e.g., Wang and Wang [15], Zhang et al. [16], Miller et al. [17,18], and Castillo et al. [19,20]. Zhang et al. [16] showed that the OPD is mainly caused by wake structures, as well as by log-layer structures. The OPD contribution from the viscous sublayer and buffer layer structures is rather small. These findings suggest that for high-Reynolds-number flows, wall-modeled large-eddy simulations (WMLESs) can constitute an accurate and efficient technique for predicting the aero-optical distortions [15]. Recent analyses by Miller et al. [17] suggest that the balance of the OPD contributions from the different parts of the boundary layer depends on the freestream Mach number, and this dependence is investigated further in this paper. Additional dependencies, such as on the wall-to-recovery temperature ratio, are also being investigated [13,21].

Information about the boundary-layer density fluctuations is required to quantify the OPD [22]. This information can be obtained from DNS, LES, or measurements. The accurate simulation of compressible high-Reynolds-number boundary-layer flows is challenging and computationally expensive. By resolving all scales of fluid motion, DNS provides high-fidelity reference data. However, for most practical applications, the computational cost is prohibitive. Choi and Moin [23] estimate the required number of grid points for DNS as $N \approx Re_L^{37/14}$. In LES, the large energy-bearing flow structures are resolved, while the smaller, more isotropic dissipating flow structures are modeled with a subgrid stress (SGS) model. According to Choi and Moin [23], the number of grid points for wall-resolved LES scales as $N \approx Re_L^{13/7}$. For example, Tromeur et al. [9] carried out LES of compressible boundary-layer flows at subsonic and supersonic Mach numbers and investigated the suitability of LES for the prediction of aero-optical aberrations. For boundary-layer flows, the computational expense of LES can be further reduced by resolving only the energy-bearing structures in the outer layer and modeling the inner layer. This approach is referred to as WMLES. Compared to wall-resolved LES, the near-wall grid line spacing and the time step can be larger, which further reduces the computational expense. According to Choi and Moin [23], the number of grid points for WMLES scales with $N \approx Re_L$. Wall-models were proposed, e.g., by Yang et al. [24] and Catchirayer et al. [25]. Successful WMLES of external flows were carried out by, e.g., Bocquet et al. [26] and Kawai and Larsson [27].

The OPD of subsonic and supersonic flows has been investigated in both experiments (e.g., [12–14,28,29]) and simulations (e.g., [9,15]). Building on the strong Reynolds analogy (SRA) (which makes a connection between the velocity and temperature field), the "linking equation" from Sutton's statistical model [22,30], and the adiabatic wall assumption, researchers at the University of Notre Dame developed a scaling law for the OPD (herein referred to as the Notre Dame [ND] model [11–13]). According to this model, OPD depends on the freestream density, the boundary-layer thickness, the freestream Mach number, and the local skin friction coefficient. A rather limited number of experiments (e.g., [14]) and simulations (e.g., [17–20]) have provided measurements of the OPD for hypersonic Mach numbers. While other studies (e.g., [12,13,28,29]) have shown that the ND model is sufficiently accurate up to freestream Mach numbers of about five, discrepancies begin to appear for hypersonic Mach numbers. For higher Mach numbers, the cause of these discrepancies may be related to the underlying model assumptions that are no longer valid or additional flow physics may not be captured in the current model. Elucidation of these effects is a primary goal of the current work.

This paper reports on WMLES of turbulent flat-plate boundary-layer flows for freestream Mach numbers of $M_\infty = 3.5$, 7.87, and 13.64. Aspects of the $M_\infty = 7.87$ simulation were discussed in Ref. [21]. The objectives of the current work are to evaluate the ND model at large hypersonic Mach numbers, to evaluate the underlying model assumptions, and to uncover new flow physics. First, the governing equations are introduced. Next, mean flow profiles, Reynolds stress profiles, root-mean-square (RMS) OPD values, and two-point correlations obtained from the WMLES are compared with reference data from DNS [16–18,31] and experiments [14]. Particular attention is paid to the effect of the freestream Mach number on the underlying assumptions of the ND model [11–13]. Finally, the time-dependent density field was analyzed with the proper orthogonal decomposition (POD).

II. Methodology

WMLESs of compressible flat plate turbulent boundary layers were carried out for three different Mach numbers.

A. Simulation Strategy

The simulations were carried out with a finite-volume compressible Navier–Stokes code with ninth-order-accurate convective terms, fourth-order-accurate viscous terms, and second-order-accurate time integration [32,33]. Details about the wall model are provided by Kawai and Larsson [27]. The SGS was obtained from the wall-adapting local eddy-viscosity (WALE) model by Nicoud and Ducros [34]. No-slip and no-penetration conditions were enforced at the wall. The wall was either adiabatic (zero wall-normal temperature gradient) or isothermal (fixed temperature). Flow periodicity was enforced in the spanwise direction. Dirichlet conditions were enforced at the inflow and freestream boundaries, and Neumann conditions were employed at the outflow boundary.

B. Reference Parameters and Nondimensionalization

All flow quantities were made dimensionless. An arbitrary reference scale, L^*_{ref}, was chosen for making length scales dimensionless. The reference length scale was $L^*_{\text{ref}} = 0.027$, 1, and 1.232 m for the $M_\infty = 3.5$, 7.87, and 13.64 cases, respectively. The freestream velocity was taken as reference velocity u^*_∞. Density was made dimensionless by the freestream density ρ^*_∞. Temperature and pressure were made dimensionless with the freestream temperature (T^*_∞) and $\rho^*_\infty u^{*2}_\infty$, respectively. Time was normalized by $L^*_{\text{ref}}/u^*_\infty$. The laminar and subgrid viscosity, μ and μ_T, were made dimensionless with μ^*_∞. The laminar and turbulent Prandtl numbers were 0.71 and 0.9, respectively.

C. Computational Domain

Using algebraic functions, a computational grid was generated for the WMLES. A grid resolution study was performed for $M_\infty = 7.87$ [21] to determine the minimum resolution for obtaining mean profiles and turbulence statistics that matched reference DNS results with acceptable accuracy. The same grid is employed for the present

WMLESs. The rescaling and recycling method by Stolz and Adams [35] was employed to sustain the turbulent approach flow boundary layer. The dimensions of the computational grid are $1.2288 \times 0.338 \times 0.12$ in the streamwise, wall-normal, and spanwise directions, respectively. The number of cells in the three directions is $512 \times 64 \times 160 = 5.24 \times 10^6$. For this grid resolution, good agreement of the skin-friction coefficient, mean velocity and temperature, and turbulence statistics with reference DNS data [16] was obtained (see Sec. III). Following suggestions by Larsson et al. [36], for an estimated boundary-layer thickness of $\delta \approx 0.06$, a wall-normal grid line spacing of $\Delta y/\delta = 0.02$ was employed between the wall and $y/\delta = 0.2$. The wall-normal grid line spacing at the boundary-layer edge is no more than $\Delta y/\delta = 0.05$. Outside the near-wall region ($y/\delta \leq 0.2$), the wall-normal grid line stretching is 5% and decreases away from the wall. The near-wall grid line spacing in wall-units is $\Delta x^+ \approx (35, 39, 41)$, $\Delta y^+ \approx (9, 10, 10)$, and $\Delta z^+ \approx (11, 12, 12)$ in the streamwise, wall-normal, and spanwise directions for $M_\infty = (3.5, 7.87, 13.64)$.

D. Flow Properties and Simulation Parameters

The freestream and wall-temperature conditions for all cases are summarized in Table 1. Also included in the table are the Reynolds number based on the reference length, Re; the Reynolds number based on inflow momentum thickness, $Re_{\theta,\text{in}}$; and the Reynolds number based on friction velocity, Re_τ, for $x = 1.1$. In the table, $T_r = T_\infty[1 + 0.5r(\gamma - 1)M_\infty^2]$, is the recovery temperature with recovery factor $r \approx \sqrt[3]{Pr} = 0.89$. The Mach 3.5 case matches the conditions of a DNS by Barone et al. [31] that was further analyzed by Miller et al. [17]. The Mach 8 conditions match those inside the SNL Hypersonic Wind Tunnel (HWT), as reported by Zhang et al. [16] and Miller et al. [17,18]. For the Mach 14 case, the conditions of the Arnold Engineering Development Complex (AEDC) Hypervelocity Tunnel 9 are matched [16]. The working gas for cases 1 and 3 is air, and the viscosity was obtained from Sutherland's law. The Mach 8 experiment was carried out with nitrogen, and the viscosity was calculated with Keyes law [37]. For the chosen conditions, high-temperature gas effects are insignificant, and the perfect gas equation was used to model the gas behavior.

The simulations were advanced in time until the flow became statistically stationary. Then time averages and statistical quantities were computed over time intervals of $t_{\text{avg/stat}}$. The time intervals and computational time step, Δt, for the different cases, made dimensionless by $L^*_{\text{ref}}/u^*_\infty$, are provided in Table 2. Profiles of the time-averaged and statistical data were extracted at $x = 1.1$ and averaged in the homogeneous spanwise direction.

E. Optical Path Length and Optical Path Difference

To investigate the effect of the density gradients on the optical aberrations, the density fields were first converted into index-of-refraction, n, fields via the linear Gladstone–Dale relation [38]:

$$n(x, y, z, t) = 1 + K^*_{\text{GD}}\rho^*(x, y, z, t) \tag{1}$$

where $K^*_{\text{GD}} = 2.3527 \times 10^4$ m^3/kg is the Gladstone–Dale constant for nitrogen over the pressure and temperature range of the present simulations [39,40]. Wall-normal integration of the index of refraction from the wall to the freestream provides the optical path length:

$$\text{OPL}(x, z, t) = \int_0^y n(x, y, z, t)\,\mathrm{d}y \tag{2}$$

Table 2 Time intervals for computation of time averages, statistical data, OPL, and computational time step

Case	$t_{\text{avg/stat}}$	t_{OPL}	Δt
1	17.5	7.5	0.0005
2	12.5	7.5	0.0005
3	15.0	7.5	0.0005

The aperture is defined as the x and z range over which the OPD is computed. Fluid structures on the order of the aperture size distort the optical wavefront [41]. Boundary-layer growth tilts the beam. Finally, mechanical vibration of the experimental components can introduce errors in the analysis of wavefront images [42]. Therefore, the mean tip and tilt of the beam are accounted for using a correction made at each time instant:

$$\text{OPD}(x, z, t) = \text{OPL}(x, z, t) - (m_x x + m_z z + b) \tag{3}$$

Following Wang and Wang [15], the coefficients are determined from a planar least-squares fit over an aperture:

$$R = \int_x \int_z [\text{OPL}(x, z, t) - (m_x x + m_z z + b)]^2\,\mathrm{d}x\,\mathrm{d}z \tag{4}$$

The minimization of Eq. (4) leads to a system of equations that is solved for the unknowns m_x, m_z and b, which are referred to as streamwise tilt, spanwise tilt, and piston components, respectively. The RMS streamwise and spanwise tilt depend on the aperture size [41]. As the aperture size exceeds the boundary-layer thickness, the tilt introduced by individual boundary-layer structures is averaged out more, and the overall tilt is smaller.

In the study of aero-optical properties of turbulent boundary layers, the overall OPD_{rms} is often considered:

$$\text{OPD}_{\text{rms}} = \sqrt{\overline{\langle \text{OPD}^2(x, z, t)\rangle}} \tag{5}$$

where the angular brackets denote spatial averaging over the aperture and the overbar denotes temporal averaging. In this paper, the OPD_{rms} obtained from the simulations is compared with a relationship proposed by Gordeyev et al. [11]:

$$f(M_\infty) = \frac{\text{OPD}_{\text{rms}}}{K_{\text{GD}}\rho_\infty c_f^{0.5} M_\infty^2 \delta} \tag{6}$$

which is referred to here as the ND model. This model is built on a theoretical framework that includes an equation by Sutton for the wavefront-distortion statistics [22,30], which is known as the "linking equation":

$$\text{OPD}^2_{\text{rms}} = 2K^2_{\text{GB}} \int_0^L \rho^2_{\text{rms}}(y)\Lambda_\rho(y)\,\mathrm{d}y \tag{7}$$

An important component of the former relationship that is also studied herein is the correlation length of the fluctuating density field in the light propagation direction:

Table 1 Freestream and wall-temperature conditions, and Reynolds numbers

Case	M_∞	u^*_∞, m/s	ρ^*_∞, kg/m^3	T^*_∞, K	T^*_w, K	T_w/T_r	Re	$Re_{\theta,\text{in}}$	Re_τ
1	3.5	1144.4	0.863450	264.9	Adiabatic	1.0	1.60×10^6	1907	592
2	7.87	1154.6	0.026018	51.8	298	0.478	8.16×10^6	9714	772
3	13.64	1882.9	0.017001	47.4	300	0.185	12.0×10^6	14408	932

Downloaded by University of Notre Dame on January 23, 2025 | http://arc.aiaa.org | DOI: 10.2514/1.J064115

$$\Lambda_\rho(y) = \frac{1}{2}\int_{-y}^{L-y} R_{\rho\rho}(y, \Delta y)\, \mathrm{d}\Delta y \tag{8}$$

where the two-point density correlation is defined as

$$R_{\rho\rho}(y, \Delta y) = \frac{\overline{\langle \rho'(x, y, z, t)\rho'(x, y + \Delta y, z, t)\rangle}}{\sqrt{\overline{\langle \rho'^2(x, y, z, t)\rangle}}\sqrt{\overline{\langle \rho'^2(x, y + \Delta y, z, t)\rangle}}} \tag{9}$$

F. Proper Orthogonal Decomposition

The POD by Lumley [43] is often utilized for the analysis of turbulent flows. Typically, the computationally efficient "snapshot" method by Sirovich [44,45] is employed. The POD provides a compact representation (least number of modes required) of unsteady flows. For incompressible flows, the POD kernel is based on two times the kinetic energy, and the POD captures more of the kinetic energy of a time-dependent flowfield than other decompositions. Rowley et al. [46] proposed a kernel for the POD of compressible flows:

$$u_i u_j + \frac{2\alpha}{\gamma - 1} c_i c_j \tag{10}$$

where $c = \sqrt{\gamma RT}$, with $R = 1/(\gamma M_\infty^2)$, is the speed of sound. For $\alpha = 0$, the incompressible kernel is recovered. For $\alpha = 1/\gamma$, the kernel is identical to two times the total internal energy; for $\alpha = 1$, the kernel is identical to two times the total enthalpy. For the present work, the interest is on the optical distortions that are caused by density fluctuations. Therefore, in addition, a third density-based kernel,

$$\rho_i \rho_j \tag{11}$$

was considered.

The POD modes are orthogonal and sorted according to their eigenvalue magnitude. The POD eigenvalue magnitude is identical to twice the kinetic energy ($\alpha = 0$), the total internal energy ($\alpha = 1/\gamma$), total enthalpy ($\alpha = 1$), or the square of the density fluctuations (for density-based kernel) of the respective modes. The instantaneous flow data can be reconstructed from the time coefficients, $a_i(t)$, and POD modes, $\boldsymbol{q_i}(\boldsymbol{x})$, according to

$$\boldsymbol{v}(\boldsymbol{x}, t) = \sum_i a_i(t)\boldsymbol{q_i}(\boldsymbol{x}) \tag{12}$$

III. Mean Flow and Statistics

The compressible displacement thickness δ^*, momentum thickness θ, and incompressible shape factor H_i are plotted in Fig. 1a. The incompressible shape factor asymptotically approaches a value of 1.4, which is inside the commonly accepted range for turbulent boundary layers ($1.3 \leq H_i \leq 1.4$).

Density-weighted van Driest–transformed velocity profiles,

$$u^{\mathrm{VD}} = \int \sqrt{\frac{\rho}{\rho_w}}\, \mathrm{d}u^+ \tag{13}$$

for $x = 1.1$ are plotted in Fig. 1b. The dashed parts of the profiles were obtained directly from the wall model. The matching point (for the wall model) is at $y^+ \approx 50$ and is well within the log-layer. The profiles are in good agreement with the relationships for the viscous sublayer, $u^+ = y^+$, and the log layer, $u^+ = 5.2 + \ln(y^+)/0.41$ (dotted and dashed black lines in Fig. 1b).

Velocity and temperature profiles for $x = 1.1$, computed from the temporal and spanwise averages of the flowfields, are plotted in Fig. 2. For comparison, profiles from DNS by Miller et al. [17] and Zhang et al. [16] are included. In this and all following figures, the dashed orange lines indicate the wall model matching point location.

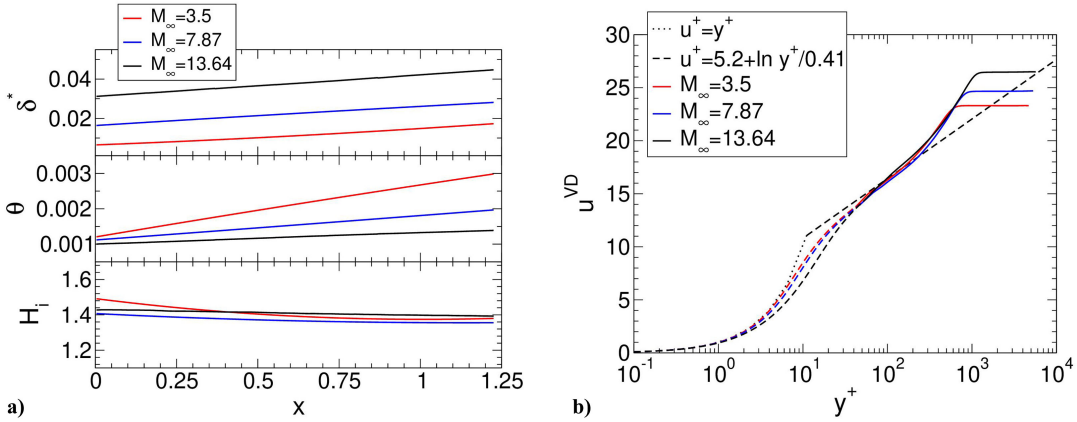

Fig. 1 a) Compressible displacement and momentum thickness as well as incompressible shape factor. b) Velocity profiles in wall units.

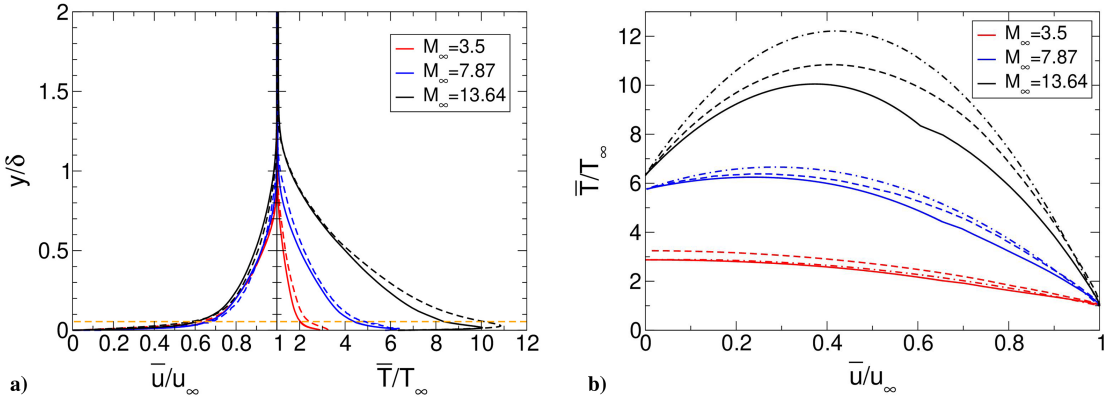

Fig. 2 Mean velocity and temperature profiles plotted against a) normalized wall distance and b) against each other (——, WMLES; - - -, DNS [16,17]; – – –, Walz [47]).

Downloaded by University of Notre Dame on January 23, 2025 | http://arc.aiaa.org | DOI: 10.2514/1.J064115

The RMS error of the velocity and temperature profiles relative to the reference DNS [16,17],

$$E_{\text{rms}}(a) = \sqrt{\frac{\sum(1/2)(y_j - y_{j-1})\left[\left(a_j^{\text{LES}} - a_j^{\text{DNS}}\right)^2 + \left(a_{j-1}^{\text{LES}} - a_{j-1}^{\text{DNS}}\right)^2\right]}{\sum(y_j - y_{j-1})}} \tag{14}$$

was computed from the wall-model interface to the boundary-layer edge. In Eq. (14), the subscript j refers to the grid nodes, y refers to the wall-normal coordinate, and a refers to the variable under consideration (i.e., $\overline{u}$ or $\overline{T}$). Good agreement between the WMLES and DNS mean velocity profiles is obtained for all cases (Table 3). For $M_\infty = 3.5$ and $M_\infty = 13.64$, the mean temperature near the wall is slightly colder compared to the reference DNS.

In Fig. 2b, the temperature is plotted versus the velocity and compared with a relationship from Walz [47]:

$$\frac{\overline{T}}{T_\infty} = \frac{T_w}{T_\infty} + \frac{\overline{u}}{u_\infty}\left(\frac{T_r - T_w}{T_\infty}\right) + \left(\frac{\overline{u}}{u_\infty}\right)^2\left(\frac{T_\infty - T_r}{T_\infty}\right) \tag{15}$$

The agreement between the curves obtained from the WMLES and the Walz relationship [47] is good for the supersonic case and adequate for $M_\infty = 7.87$ and $M_\infty = 13.64$. The irregularity near $\overline{u}/u_\infty = 0.6$ is located at the wall-model interface and can be attributed to a slight mismatch between the wall model solution and the WMLES mean flow. According to Duan et al. [48] and Zhang et al. [16], as the wall temperature decreases, the mismatch between the Walz relationship [47] and the simulations increases. The present results are consistent with the former statement. The largest mismatch between the computed and predicted (Walz) temperature distribution is obtained for the $M_\infty = 13.64$ cold wall case.

Table 3 Mean velocity and temperature profiles' RMS error relative to reference DNS [16,17]

M_∞	$E_{\text{rms}}(\bar{u})$	$E_{\text{rms}}(\bar{T})$
3.5	0.0039	0.0875
7.87	0.0056	0.1275
13.64	0.0074	0.3346

The resolved RMS velocity fluctuations in the streamwise, wall-normal, and spanwise directions are compared in Fig. 3. For the hypersonic cases, the profiles are normalized by the friction velocity to allow for direct comparison with the published data. The streamwise fluctuation profiles are in good agreement with the reference DNS [16–18]. Similarly good agreement of the wall-normal and spanwise fluctuation profiles is observed for Mach 3.5. For Mach 8 and 14, the wall-normal and spanwise fluctuation profiles are in qualitative agreement with the DNS. In the LES, the magnitude of the resolved velocity fluctuations depends on the grid resolution and the SGS model. Therefore, the resolved RMS fluctuations in the WMLES are expected to be lower than the (total) fluctuations in the DNS.

The RMS fluctuations of the thermodynamic quantities, normalized by the local mean density, temperature, and pressure, are plotted in Fig. 4. The distributions obtained from the WMLES (solid lines) are in adequate qualitative agreement with the distributions obtained from the reference DNS [16,18] (dashed lines). With increasing Mach number, the overall magnitude of the fluctuations increases, and the peaks of the density and temperature fluctuations shift away from the wall and toward the boundary-layer edge. The pressure fluctuations within the boundary layer are much lower than the density and temperature fluctuations [49] but increase with Mach number. DNSs by Zhang et al. [50] indicated a strong increase of the turbulent pressure fluctuations with Mach number both near the wall and above the boundary layer.

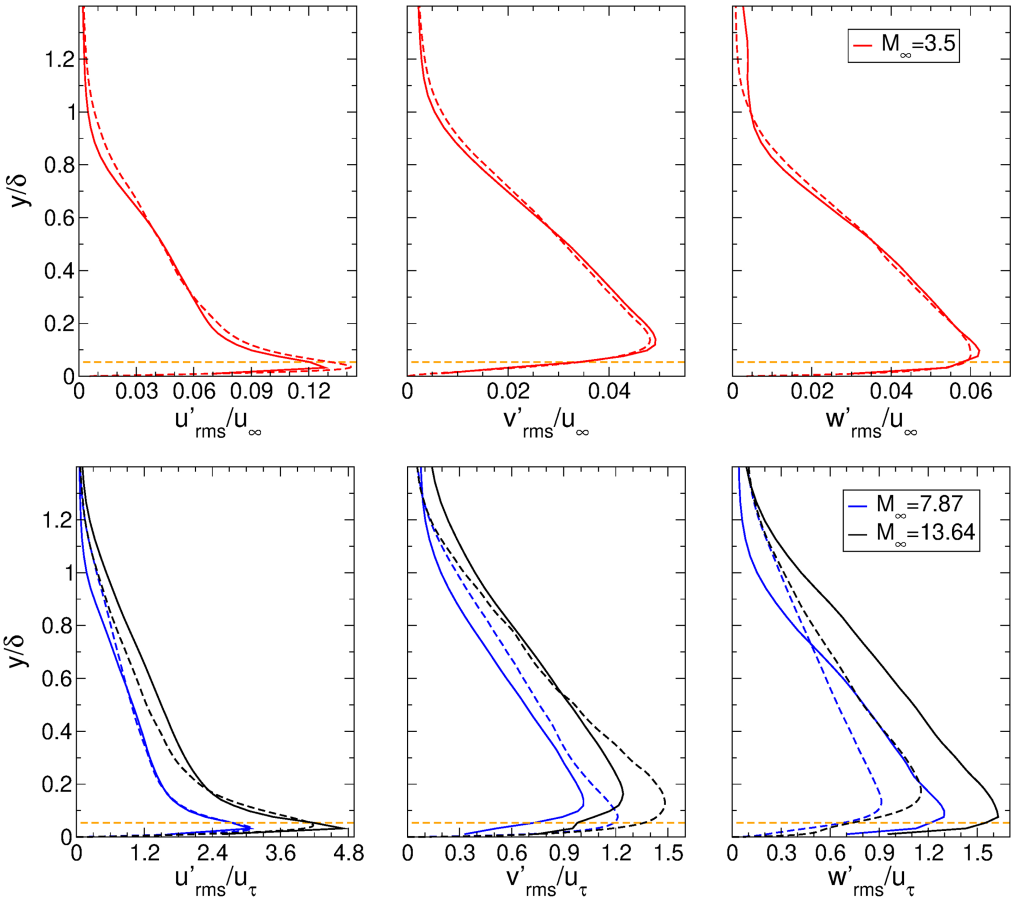

Fig. 3 Profiles of resolved root-mean-square velocity fluctuations (——, WMLES; - - -, DNS [16,17]).

Downloaded by University of Notre Dame on January 23, 2025 | http://arc.aiaa.org | DOI: 10.2514/1.J064115

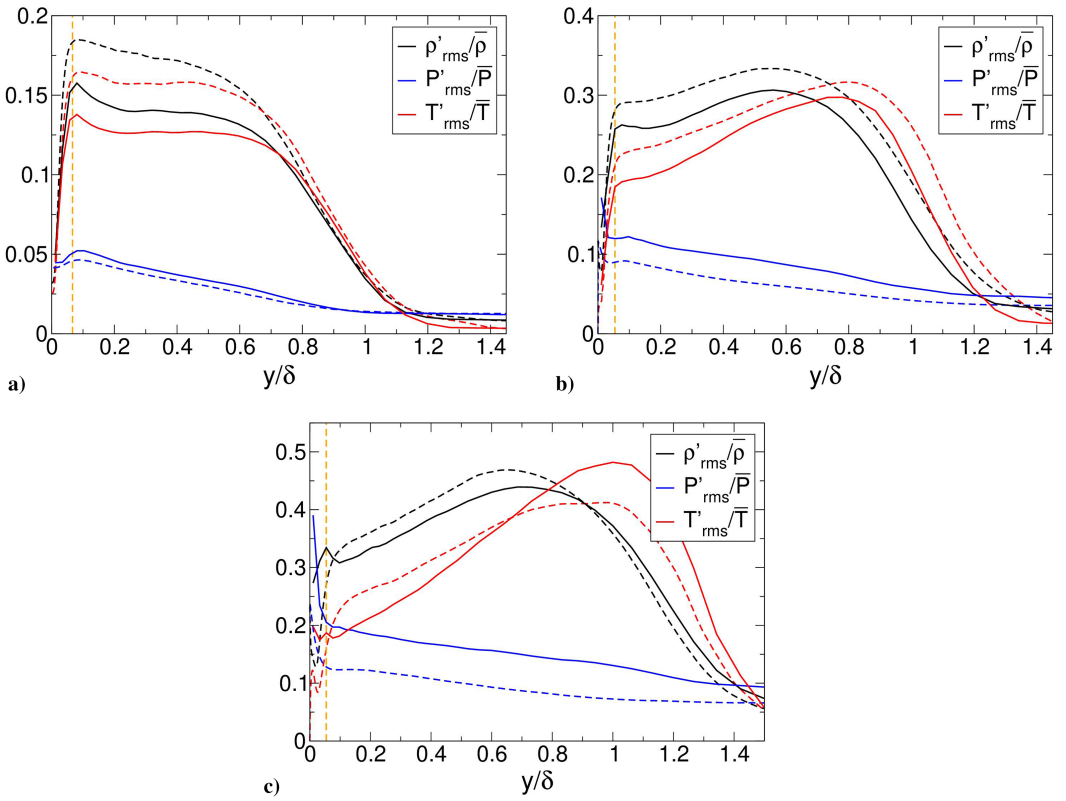

Fig. 4 Root-mean-square fluctuations of thermodynamic variables for a) $M_\infty = 3.5$, b) $M_\infty = 7.87$, and c) $M_\infty = 13.64$ (—, WMLES; ---, DNS [16,18]).

IV. Aero-Optical Characterization

The instantaneous density fields were saved every five time steps. The OPL was collected over time intervals of t_{OPL} (Table 2). A total of 3000 density fields were saved, and the OPL was computed for an aperture with streamwise and spanwise extents of $Ap_x \times Ap_z \approx 6\delta \times 3\delta$ [15]. Figure 5 shows the normalized OPD, $f(M_\infty)$ from Eq. (6), plotted against the ND model relationship [29,51], as well as previously published numerical (e.g., [17,18]) and experimental data (e.g., [14,29,51]). The $f(M_\infty)$ for the different cases are also provided in tabular form (Table 4). The values obtained from the present WMLES are in reasonable agreement with the published data (1.53% error for $M_\infty = 3.5$, 1.25% for $M_\infty = 7.87$, and 12% for $M_\infty = 13.64$, compared to numerical data). Small differences in the $\mathrm{OPD}_{\mathrm{rms}}$ can be attributed to an underprediction of the temperature near the wall (Fig. 2), which, through the equation of state, directly influences the density and thus the OPD. The modeled fluctuations in the LES do not contribute to the $\mathrm{OPD}_{\mathrm{rms}}$, which provides another argument for the lower $\mathrm{OPD}_{\mathrm{rms}}$ values compared to the DNS.

Table 4 Normalized $\mathrm{OPD}_{\mathrm{rms}}$

Method	3.5	7.87	13.64
WMLES	0.1126	0.056	0.028
DNS [17,18]	0.1109	0.056	0.025
Experiments [14]	— —	0.058	— —

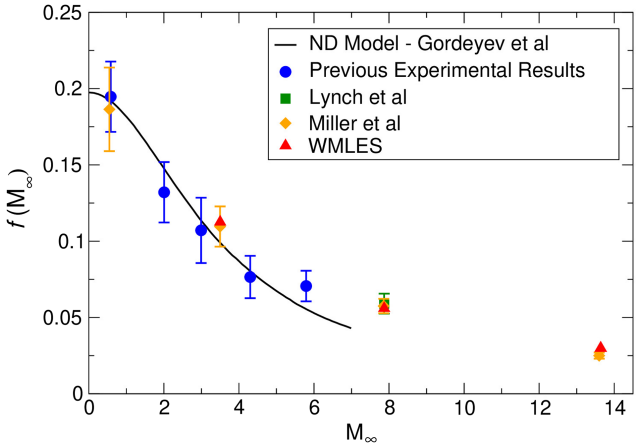

Fig. 5 Normalized $\mathrm{OPD}_{\mathrm{rms}}$. The Notre Dame model and experimental data by Gordeyev et al. [29,51], numerical data by Miller et al. [18], and experimental data by Lynch et al. [14].

Although the ND model was not intended to be used for higher Mach numbers, it appears to work well up to Mach five. This has been demonstrated earlier, both experimentally and numerically [11,13,17]. The numerical and experimental results for $5 \leq M_\infty \leq 8$ deviate from the model prediction and plateau around $f(M_\infty) \approx 0.07$. This discrepancy suggests that some of the underlying model assumptions may be violated for hypersonic flows, as previously discussed by Gordeyev and Juliano [29]. The present results also suggest that the normalized $\mathrm{OPD}_{\mathrm{rms}}$ drops again for $M_\infty > 8$.

According to Lynch et al. [14] and Miller et al. [17,18], other physical mechanisms (e.g., acoustic radiation) that are intrinsic to hypersonic flows play a role at high Mach numbers. Gordeyev and Juliano [29] surmised that the pressure fluctuations, which are small for subsonic and supersonic flows, cannot be ignored for hypersonic flows. As seen in Fig. 4, although the pressure fluctuations are much weaker than the density and temperature fluctuations, they increase with Mach number. Thus, for hypersonic flows, the pressure fluctuations will likely have to be considered. Instantaneous isocontours of the density gradient magnitude at $z = 0.6$ ("numerical schlieren" images) visualize regions of strong density gradients within the mildly growing boundary layer (Fig. 6). Most noticeable for the Mach 14 case, oblique structures or shocklets are located above the larger eddies. Such structures have been previously found for high Mach numbers and are indicative of strong acoustic radiation [50,52–54].

With increasing Mach number, the density gradients become stronger and concentrated closer to the boundary-layer edge. By integrating Eq. (2) from the wall to y, the cumulative $\mathrm{OPD}_{\mathrm{rms}}$

Downloaded by University of Notre Dame on January 23, 2025 | http://arc.aiaa.org | DOI: 10.2514/1.J064115

Downloaded by University of Notre Dame on January 23, 2025 | http://arc.aiaa.org | DOI: 10.2514/1.J064115

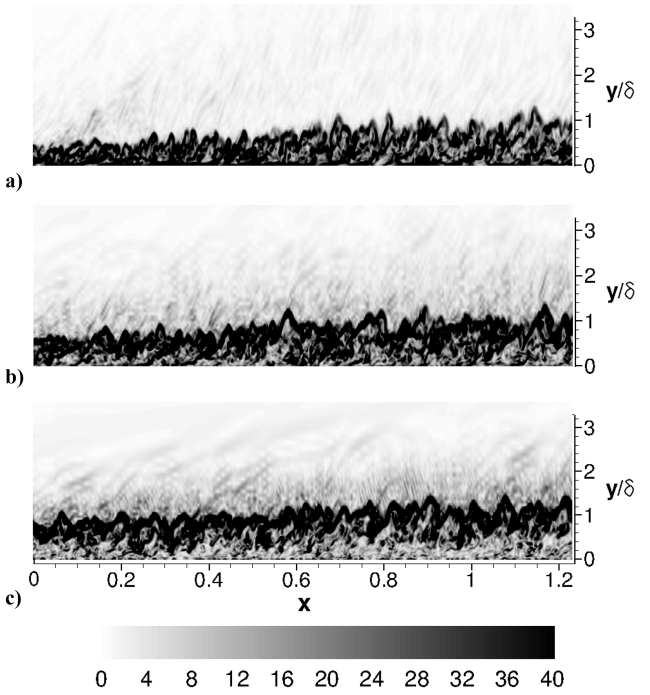

Fig. 6 Instantaneous isocontours of density gradient magnitude for a) $M_\infty = 3.5$, b) $M_\infty = 7.87$, and c) $M_\infty = 13.64$.

contribution was obtained (Fig. 7). In the figure, the cumulative OPD_{rms} contribution for each case was normalized by their respective total OPD_{rms}. The same analysis was performed by Wang and Wang [15] and Miller et al. [18]. The distributions by Miller et al. [18] are included in Fig. 7 (dashed lines). With increasing Mach number, the near-wall contribution to the total OPD_{rms} decreases, which is consistent with the shift of the density gradients to the boundary-layer edge (Fig. 4). For the hypersonic Mach numbers, the cumulative OPD_{rms} increase is higher near the boundary-layer edge.

According to Gordeyev et al. [11,12,29] the large-scale structures in the outer portion of the boundary layer have the strongest effect on the refraction index fluctuations when integrated across the boundary layer. The convection velocity of the large-scale structures was calculated as [51]

$$\frac{u_c}{u_\infty} = \frac{\int n'_{\text{rms}}(y)u(y)\,\mathrm{d}y}{u_\infty \int n'_{\text{rms}}(y)\,\mathrm{d}y} \tag{16}$$

Figure 8 compares the convection velocities computed inside the aperture with previously published experimental results by Gordeyev and Juliano [29] and Lynch et al. [14], and unpublished numerical results taken from the four DNS datasets reported in Miller et al. [18]. The convection velocities obtained from the present WMLES are summarized in Table 5. Results are in good agreement with the reference DNS data. Measurements by Lynch et al. [14] suggest a convection velocity of approximately 0.87 (of the freestream velocity) at $M_\infty = 7.87$. For $M_\infty < 6$, the convection velocity increases monotonically with the Mach number. The present results follow this trend.

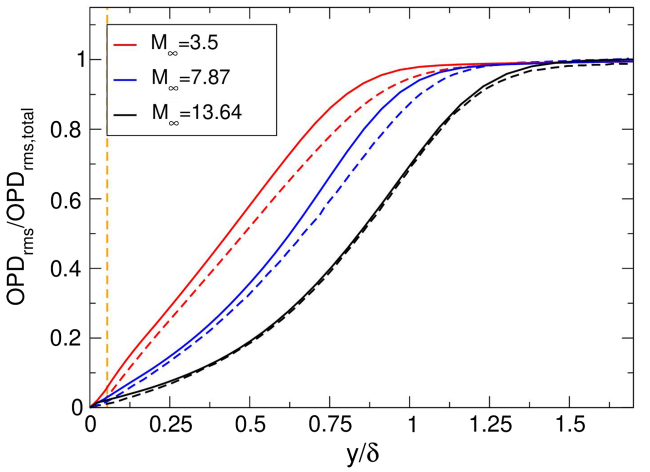

Fig. 7 Cumulative contribution to total OPD_{rms} as a function of the wall-normal distance (——, WMLES; - - -, DNS [18]).

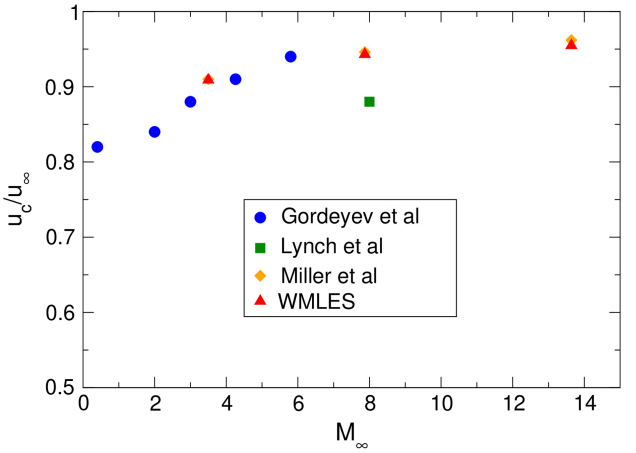

Fig. 8 Convection velocity normalized by freestream velocity. Experimental data by Gordeyev and Juliano [29] and Lynch et al. [14], and numerical data from Miller et al. [18].

Table 5 Convection velocity of large-scale structures

Method	3.5	7.87	13.64
WMLES	0.91	0.94	0.95
DNS [18]	0.91	0.94	0.96
Experiments [14]	——	0.87	——

A. Reynolds Analogies

The ND model makes use of the SRA [55], which assumes a direct relationship between the heat transfer and momentum exchange. Morkovin [55] showed that the SRA can also be applied to compressible turbulent boundary layers. For the SRA in its simplest form,

$$c_p T' = -\overline{u}_i u'_i \tag{17}$$

the temperature and velocity fluctuations are perfectly anticorrelated. However, this is only true when the pressure and total temperature fluctuations are negligible [1,48,56–58].

Equation (17) suggests a linear relationship between the temperature and velocity RMS fluctuations. A scaling function,

$$A(y) = \frac{7}{4} - \frac{1}{(5/4)(y/\delta)^4 + (4/3)} \tag{18}$$

can be added to account for the shear-stress distribution [1,17]:

$$T'_{\text{rms}}(y) = \frac{A(y)\overline{u}(y)u'_{\text{rms}}(y)}{c_p} \tag{19}$$

This form of the SRA is for adiabatic walls. Extended versions of the SRA have been developed that account for wall-cooling effects. For example, a relatively simple extended SRA (ESRA) can be obtained by linearizing the Walz equation and applying the RMS operator:

$$T'_{\text{rms}}(y) = u'_{\text{rms}}(y)\left(\frac{A(y)\overline{u}(y)}{c_p} - \frac{T_r - T_w}{u_\infty}\right) \tag{20}$$

Here, T_r is the recovery (adiabatic) wall temperature.

The RMS temperature fluctuations (obtained directly from the simulations) along with the predictions obtained from the adiabatic SRA and the nonadiabatic extended SRA [21] are plotted in Figs. 9a–9c. The SRA relationship is independent of the wall temperature (only works for adiabatic wall conditions) and overpredicts the temperature fluctuations for the cooled-wall cases. The ESRA is a function of the wall temperature and displays the correct trend for the hypersonic Mach numbers (reduction of temperature fluctuations with wall cooling). However, the temperature fluctuations are still overpredicted.

The SRA assumes a perfect anticorrelation between the velocity and temperature fluctuations (i.e., $R_{u'T'} = -1$). Fluctuations of T' resulting from state variables other than u' are neglected [17]. Normalized correlations of the streamwise velocity and temperature fluctuations were computed from the WMLES data and are presented in Fig. 9d. Anything to the left of the dashed line (matching point) in Fig. 9d comes from the wall model, so it is assumed to be poorly resolved. Independent of the Mach number, the correlation is approximately $R_{u'T'} = -0.6$ throughout most of the boundary layer and is trending toward zero at the boundary-layer edge. Near the wall, the correlation increases from $R_{u'T'} \approx -0.6$ to -0.8. Guarini et al. [57], Duan et al. [48], and Maeder et al. [59] also observed a near-wall peak of $R_{u'T'} \approx -0.8$. At the wall, for the cooled wall cases, the correlation is positive, as also shown by Duan et al. [48].

A suggested fix to the ESRA is to account for the dependence of T'_{rms} on state variables other than u' [17,18]. Toward that end, the ESRA profiles for the hypersonic cases were multiplied by the negative of the corresponding $R_{u'T'}$ profiles (Figs. 9b and 9c). With this modification, the agreement of the ESRA predictions with the temperature fluctuations obtained directly from the WMLES is improved. It should be mentioned that many different Reynolds analogies were proposed in the literature over the years [60–63]. Among them, the generalized Reynolds analogy (GRA) by Zhang et al. [64] is known to give very accurate predictions for a wide range of Mach numbers and wall-cooling conditions.

B. Density Correlation Length

In Fig. 10a, two-point density correlations are plotted for five different wall-normal locations inside the $M_\infty = 7.87$ boundary layer. The distributions peak at the reference location and drop off

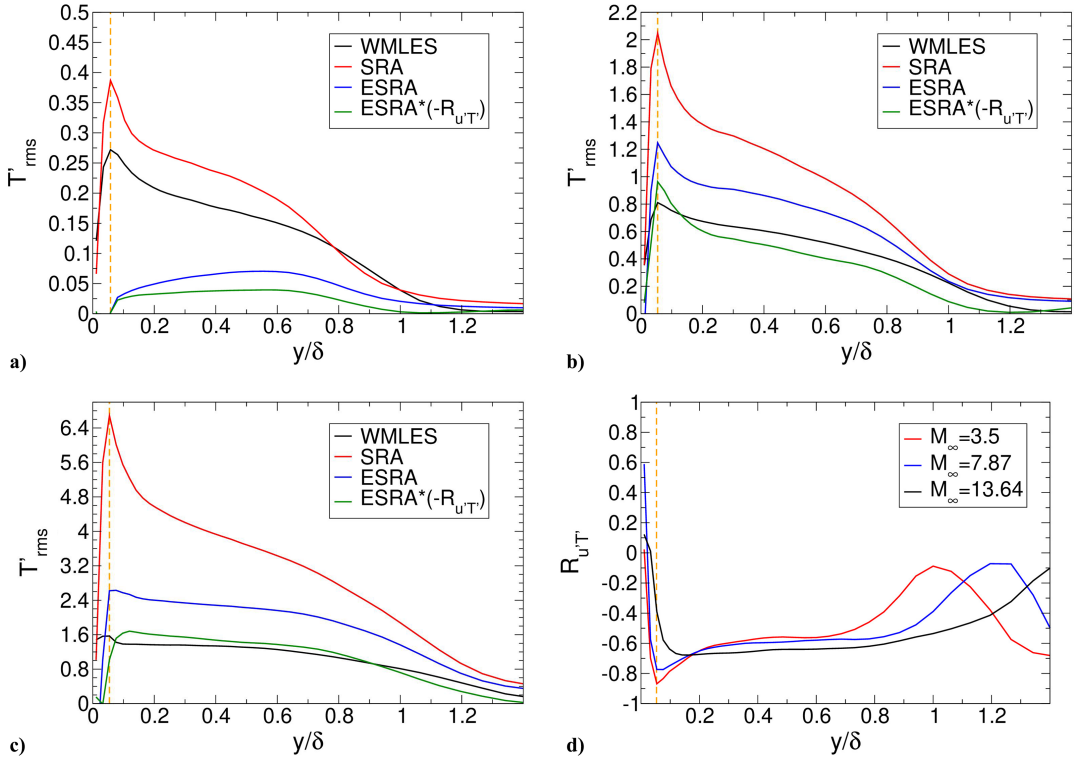

Fig. 9 Aperture-averaged temperature fluctuations and SRAs for a) $M_\infty = 3.5$, b) $M_\infty = 7.87$, c) $M_\infty = 13.64$, and d) correlations of velocity–temperature fluctuations.

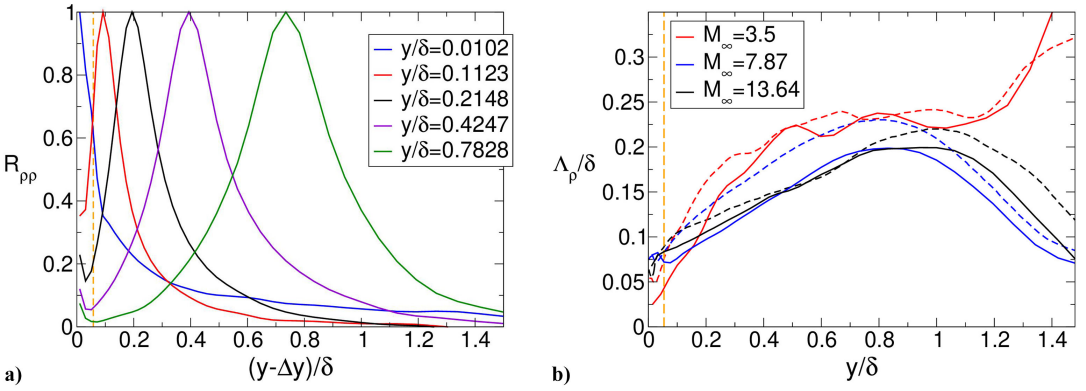

Fig. 10 a) Density correlations for five wall-normal locations ($M_\infty = 7.87$). b) Density correlation length for $M_\infty = 3.5$, $M_\infty = 7.87$, and $M_\infty = 13.64$ (——, WMLES; - - -, DNS [18]).

Downloaded by University of Notre Dame on January 23, 2025 | http://arc.aiaa.org | DOI: 10.2514/1.J064115

toward the wall and the boundary-layer edge, consistent with previously published data [9,15].

For the ND model, it is further assumed that the wall-normal density correlation length [Eq. (8)] does not depend on the Mach number. Gordeyev and Juliano [29] speculate that this assumption may not hold at high Mach numbers. Distributions of the correlation length, $\Lambda_\rho(y)$, for each case are visualized in Fig. 10b. Adequate qualitative agreement with reference DNS data by Miller et al. [18] is observed for all cases. As the Mach number increases, the peak of the correlation length moves toward the boundary-layer edge. For the adiabatic $M_\infty = 3.5$ case, the correlation length increases outside the boundary layer toward the freestream. This behavior is, however, not significant for the optical distortions, as the freestream density fluctuations are small outside the boundary layer for this case (Fig. 4).

C. Directional Dependence of Optical Distortions

Figure 11 provides two-point spatial density correlations inside the aperture for different wall-normal locations, y. For each case, 500 density snapshots spaced 0.01 time units apart were considered. In the figure, Δx and Δy are the streamwise and wall-normal distance, respectively, from the point where the beam intersects with the selected y plane. The horizontal dashed lines represent the boundary-layer edge compared to the y plane. With increasing distance from the wall, the enlargement of the correlation contours near the boundary-layer edge where structures are largest is noticeable (i.e., less concentric contour lines, tilting of contours).

For the $M_\infty = 3.5$ case, based on the 0.2 contour lines, the density correlation in the streamwise direction increases from about 0.68δ ($y/\delta = 1/3$) to 0.70δ ($y/\delta = 1$). In the wall-normal direction, it elongates from about 0.54δ ($y/\delta = 1/3$) to 0.75δ ($y/\delta = 1$).

For $M_\infty = 7.87$, the correlation length inside the boundary layer increases from about 0.66δ to 0.81δ in the streamwise direction, and from 0.52δ to 0.85δ in the wall-normal direction. For $M_\infty = 13.64$, the correlation length inside the boundary layer increases in the streamwise direction from about 0.55δ to 1.10δ, and elongates from about 0.54δ to 0.96δ in the wall-normal direction.

As the Mach number is increased, the density fluctuations correlate more strongly near the boundary-layer edge, in accordance with the previously discussed isocontours of the density gradient magnitude (Fig. 6). In addition, away from the wall and inside the boundary layer, the tilting of the contours relative to the flow direction increases, consistent with previously published data [9]. For $y/\delta = 1$, the correlation above the boundary-layer edge is inclined toward the downstream direction for the hypersonic cases.

The directionality of the OPD is best explained based on the linking equation [Eq. (8)], which depends directly on the correlation length and beam propagation distance. The correlation length is longer along an optical path tilted toward the downstream direction than toward the upstream direction [15]. For the former, the beam is more aligned with the oblique vortical flow structures, while for the latter, the beam "traverses" the flow structures. The directional dependence of the wavefront distortions is investigated by changing the inclination angle of the light beam. The inclination angle β is defined as the angle between the optical path and the freestream. For $\beta < 90$ deg, the beam is tilted in the upstream direction, and for $\beta > 90$ deg, it is tilted in the downstream direction. In the preceding paragraphs, the $\mathrm{OPD}_{\mathrm{rms}}$ values were computed for a light beam that is normal to the wall ($\beta = 90$ deg).

The dependence of the correlation length on the inclination angle β is shown in Fig. 12. The curves were obtained by second-order-accurate trapezoidal rule integration along radial lines of length δ originating from $(\Delta x, \Delta y) = (0, 0)$. The correlation length is larger for optical paths tilted toward the downstream direction. For all cases, the longest correlation lengths are obtained for inclination angles between 120 deg< β <150 deg [10], consistent with the orientation of the hairpin vortices [15,65]. Thus, larger aero-optical aberrations will be expected for downstream-tilted beams. For $M_\infty = 3.5$, the density correlation lengths are generally shorter inside the boundary layer compared to the hypersonic cases. With increasing Mach number, the correlation length inside the boundary layer increases as the boundary-layer edge is approached. The green and blue lines closely match for the higher-Mach-number case at every β, meaning that there is a strong density correlation clustered near the boundary-layer edge.

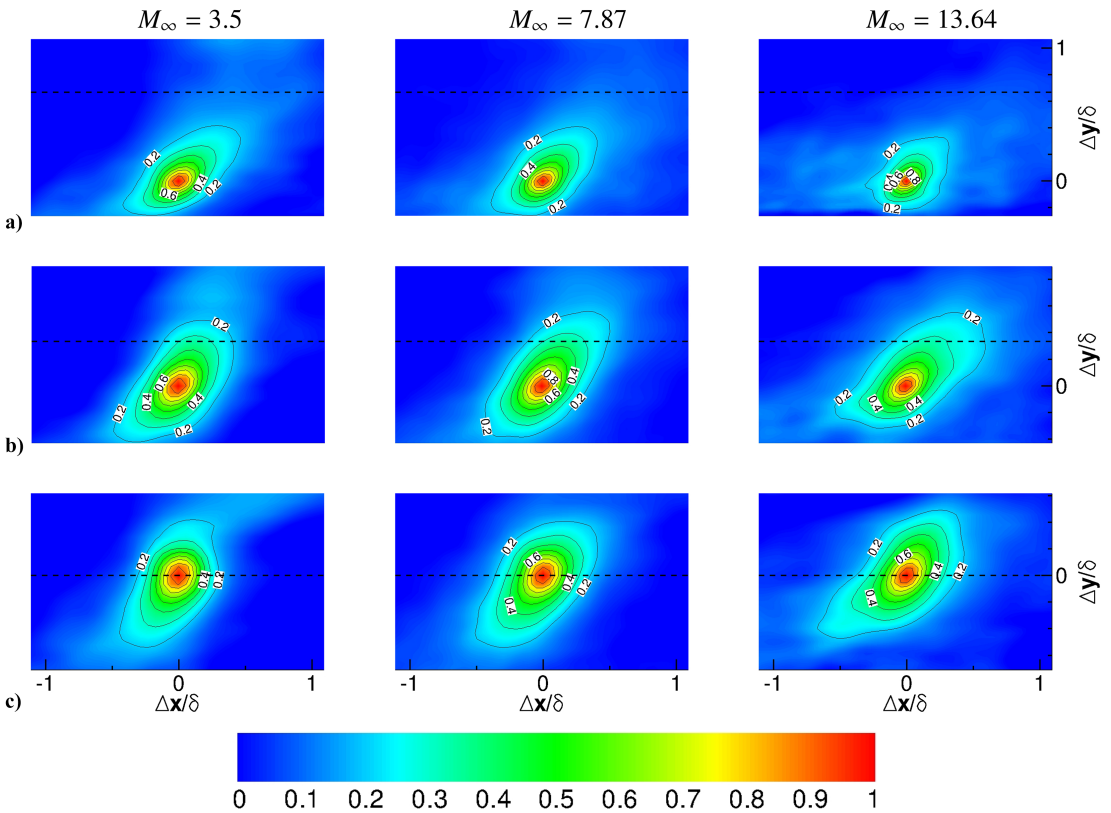

Fig. 11 Two-point correlations of density fluctuations as a function of Δx and Δy measured from the streamwise location of the beam center and a) $y/\delta = 1/3$, b) $y/\delta = 2/3$, and c) $y/\delta = 1$.

Downloaded by University of Notre Dame on January 23, 2025 | http://arc.aiaa.org | DOI: 10.2514/1.J064115

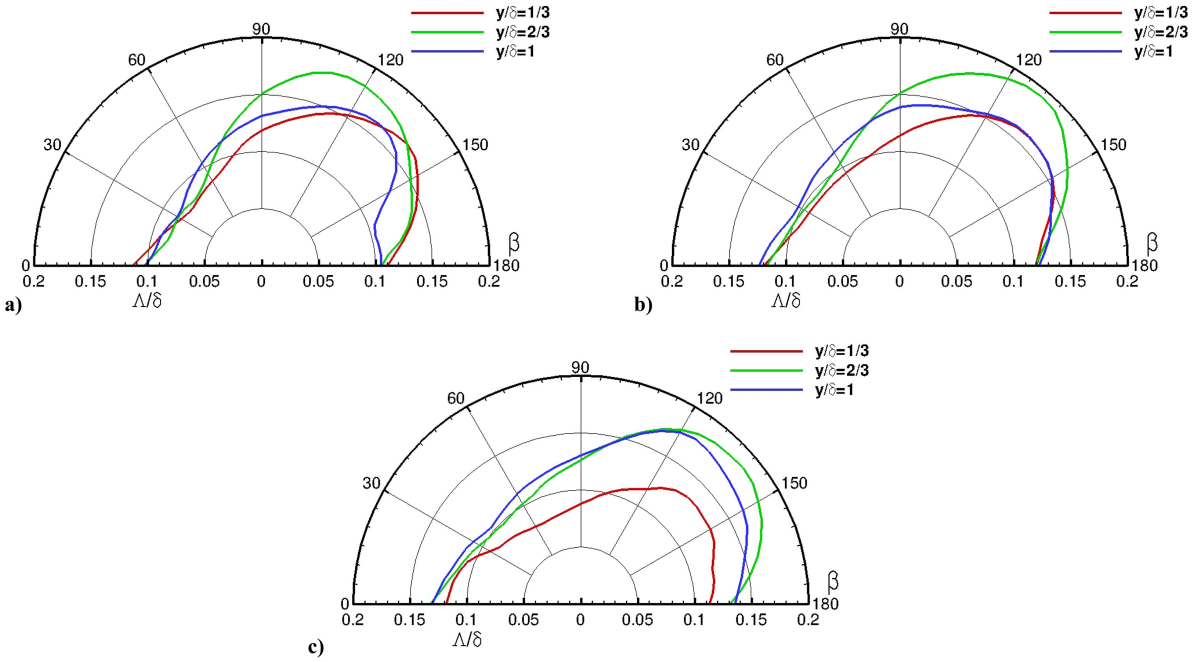

Fig. 12 Dependence of density correlation length on inclination angle for three *y*-locations and a) $M_\infty = 3.5$, b) $M_\infty = 7.87$, and c) $M_\infty = 13.64$.

D. Aperture Dependence of Beam Jitter

Jitter refers to the unsteady pointing of a beam that widens the time-averaged spot size on a target in the far field. Both aero-optical aberrations as well as mechanical vibration can contribute to beam jitter [41]. The aero-optical jitter is caused by density fluctuations over the aperture, while the mechanical jitter is directly related to mechanical vibrations. In typical experiments, it is not practically feasible to separate the aero-optical component from the mechanical component of the beam jitter. Thus, simulations are often the only alternative to isolating the aero-optical component.

In Fig. 13a, the streamwise tilt, m_x (or x-tilt), is plotted versus time for two different streamwise apertures, Ap_x. For all Mach numbers, the unsteady tilt decreases strongly when the streamwise aperture is increased from one to six boundary-layer thicknesses. As a result, the tilt removal is significantly reduced as the aperture size is increased. Similar findings were made by Wang and Wang [15] based on wall-resolved LES. It can also be observed that the magnitude of the unsteady tilt decreases significantly with increasing Mach number.

The integral or global jitter (over a rectangular or round aperture) in the streamwise direction can be defined as [41]

$$\theta_G(t;Ap) = \frac{\int_{Ap} x \cdot \mathrm{OPD}(x,z,t)\,\mathrm{d}x\mathrm{d}z}{\int_{Ap} x^2\,\mathrm{d}x\mathrm{d}z} \tag{21}$$

Lynch et al. [14] scale the global jitter with the Gladstone–Dale constant, freestream density and Mach number, skin friction coefficient, and normalized $\mathrm{OPD}_{\mathrm{rms}}$ [Eq. (6)]. The global jitter was computed for all cases for a spanwise aperture size of $Ap_z = 3\delta$ (Fig. 13b). Experimental data by Lynch et al. [14] is also included. The profile was computed using the value of $f(M_\infty)$ obtained from experiments, while the dashed line with squares from Gordeyev et al. [29] was computed using the stitching method [41]. The WMLES results are in close agreement with the experimental data profile. With increasing streamwise aperture, the beam jitter decreases sharply. In addition, the WMLES results indicate a slight increment in amplitude as the Mach number is increased. For streamwise apertures greater than 4δ, the jitter for $M_\infty = 13.64$ exceeds the jitter for $M_\infty = 3.5$.

E. Proper Orthogonal Decomposition

The different data sets for a streamwise extent representative of the aperture were analyzed with POD. A total of 500 snapshots of the flowfield, equally distributed over a time interval of $\Delta t = 5$ were considered. The POD eigenvalues, λ_i, for the different kernels are provided in Fig. 14a. Similar eigenvalue spectra were obtained for the kernels based on total energy and total enthalpy. The insert in Fig. 14a shows the eigenvalue spectra for the density-based kernel. In Fig. 14b, the sum of the leading "i_{unsteady}" eigenvalues divided by the sum over all eigenvalues,

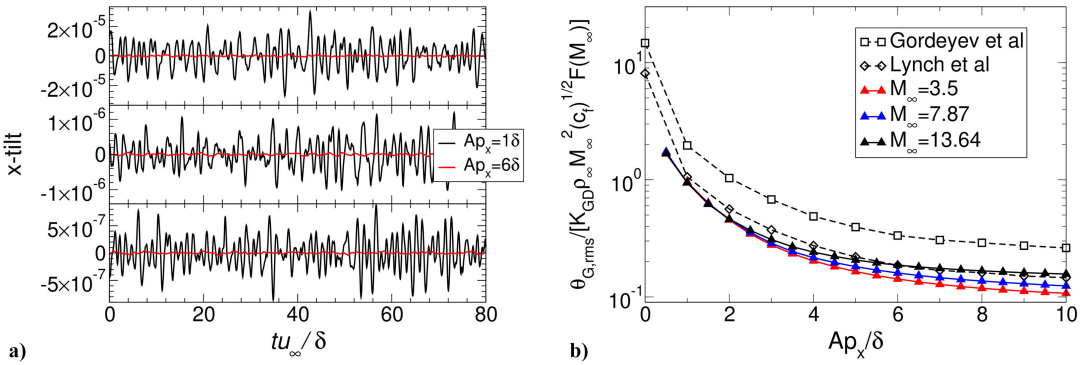

Fig. 13 a) Streamwise tilt as a function of time for $M_\infty = 3.5$ (top), $M_\infty = 7.87$ (middle), and $M_\infty = 13.64$ (bottom) and two different streamwise aperture sizes. b) Root-mean-square tilt as a function of aperture size.

Downloaded by University of Notre Dame on January 23, 2025 | http://arc.aiaa.org | DOI: 10.2514/1.J064115

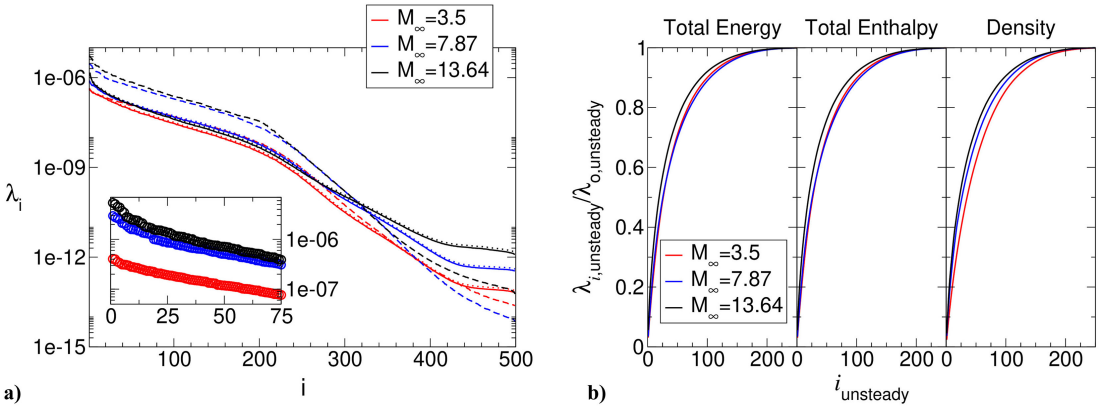

Fig. 14 a) Proper orthogonal decomposition eigenvalues (Kernel based on ——, total energy; ·····, total enthalpy; - - - and ○○○, density), and b) cumulative energy content of unsteady modes.

$$\frac{\sum_{i=1}^{i=i_{\text{unsteady}}} \lambda_i}{\sum_{i=1}^{i=i_{\max}} \lambda_i} \tag{22}$$

is plotted for the different kernels. For the density-based kernel, the eigenvalues add up more slowly. The percentage of the total unsteady energy (i.e., excluding mode 0, which is the time average) that is captured by the density-based kernel is provided in Table 6. For all cases, the leading 100 modes capture ≈90% of the total density fluctuations. This means that reconstructions based on these modes would recover almost all spatiotemporal density features of the flow. Because the interest is in the optical distortions, the density-based kernel was selected for the following analysis.

Modes 1 and 2 (first pair) represent the most dominant density fluctuations in the flowfield (Fig. 14a). Pairs of POD modes with similar shapes that are shifted in the advection direction by a quarter wave length capture traveling waves [45]. Visualizations of the leading unsteady POD modes for the different Mach numbers are provided in Fig. 15 (only one mode from each pair is shown). All coordinates were normalized by the boundary-layer thickness, which was $\delta = 0.038$ for $M_\infty = 3.5$, $\delta = 0.048$ for $M_\infty = 7.87$, and $\delta = 0.058$ for $M_\infty = 13.64$. Instantaneous density isosurfaces flooded by the density value are shown on the left. The isosurface values are noted in the bottom-right corner of the different figures. The modes capture large-scale density structures with spatial and temporal coherence. For the $M_\infty = 3.5$ case, the structures are organized in a "checkerboard" suggesting oblique waves. For the Mach 8 case, the structures appear more two-dimensional. Longitudinal structures are observed for the Mach 14 case.

Instantaneous density isocontours in a z plane are shown on the right of Fig. 15. The spanwise location of the plane was selected to most clearly visualize the mode shapes ($z/\delta(M_\infty = 3.5) = 0.00$, $z/\delta(M_\infty = 7.87) = 0.92$, and $z/\delta(M_\infty = 13.64) = 1.55$). The black dashed line represents the boundary-layer edge. For the $M_\infty = 7.87$ and 13.64 cases, the leading POD modes are located directly underneath the boundary-layer edge in agreement with the schlieren images. This behavior is consistent with the previous discussion on density correlations (refer Figs. 11a–11c) and the previously published data by Miller et al. [18]. For the $M_\infty = 13.64$ case, the dominant structures are longitudinal and noticeably extended in the streamwise direction.

For each case, the density fields were reconstructed from the leading i_{unsteady} POD modes (including mode 0, which is the time average), and the OPD_{rms} was computed following the aforementioned procedure. For sake of brevity, visualizations of the reconstructed flowfields are not provided. For all cases, the contribution to the total OPD_{rms} from the least energetic unsteady modes (i.e., beyond 300) is negligible and was disregarded in Table 7. Convergence of the OPD_{rms} is obtained faster as the Mach number is increased. The present POD analysis allows for a quantitative analysis of the effect of coherent boundary-layer structures on the OPD_{rms}.

Table 6 Density-based kernel cumulative eigenvalue magnitude (%) from leading 300 unstable-energy modes

M_∞ \ modes	25	50	100	150	200	300
3.5	39.75	62.16	85.72	95.31	98.98	99.99
7.87	48.49	68.83	88.67	96.52	99.33	99.99
13.64	53.16	73.05	90.58	97.00	99.40	99.99

V. Conclusions

WMLESs of compressible turbulent flat plate boundary layers were carried out for Mach numbers of $M_\infty = 3.5$, 7.87, and 13.64. The freestream conditions and wall-temperature ratio were matched to those of earlier DNSs [17,31] and experiments in the Hypersonic Wind Tunnel at Sandia National Laboratories and in Tunnel 9 at the Arnold Engineering Development Complex. For all cases, good agreement of the velocity profiles with reference DNS data [16,17] was obtained. In addition, good qualitative agreement of the RMS fluctuations of the velocity components and thermodynamic variables with the reference DNS data [16,17] was observed. The present simulations indicate that the pressure fluctuations within the boundary layer are weak but not truly negligible at high Mach numbers.

The OPD_{rms} obtained from the WMLES are in good agreement with published experimental and DNS data [11,13,14,17,18,29,51]. In agreement with earlier experiments and simulations [11,13,17], the normalized OPD_{rms} for the higher Mach numbers (7.87 and 13.64) is slightly larger than predictions made with a model by Notre Dame university researchers [29,51]. The model was not intended for high Mach numbers, as some of the underlying assumptions may not hold [17,18]. Nevertheless, it provides a reasonable estimate of the aero-optical distortions. The convection velocity monotonically increases with the Mach number, from $0.90u_\infty$ at $M_\infty = 3.5$ to $0.95u_\infty$ at $M_\infty = 13.64$, in agreement with previously published experimental data [14,29]. As the Mach number is increased, the density fluctuations in the outer part of the boundary layer become stronger, resulting in higher observed aero-optical convective speeds.

The SRA suggests that the streamwise velocity and temperature fluctuations are perfectly anticorrelated [55]. Independent of the Mach number, the correlation is approximately $R_{u'T'} = -0.6$ throughout most of the boundary layer and trending toward zero at the boundary-layer edge. An ESRA correction for highly cooled walls was validated. By multiplying the ESRA profiles by the negative of their respective $R_{u'T'}$ profiles, the dependence on state variables other than u' is accounted for. Additional extensions for high-Mach-number flight in the atmosphere will likely also be required, as dissociation will lead to strong density fluctuations.

The bulk contribution to the total OPD_{rms} shifts toward the boundary-layer edge as the Mach number is increased. The correlation length increases toward the boundary-layer edge, while it decreases in the outer region. The effect of the relative inclination angle of the light beam with respect to the boundary layer on the

Downloaded by University of Notre Dame on January 23, 2025 | http://arc.aiaa.org | DOI: 10.2514/1.J064115

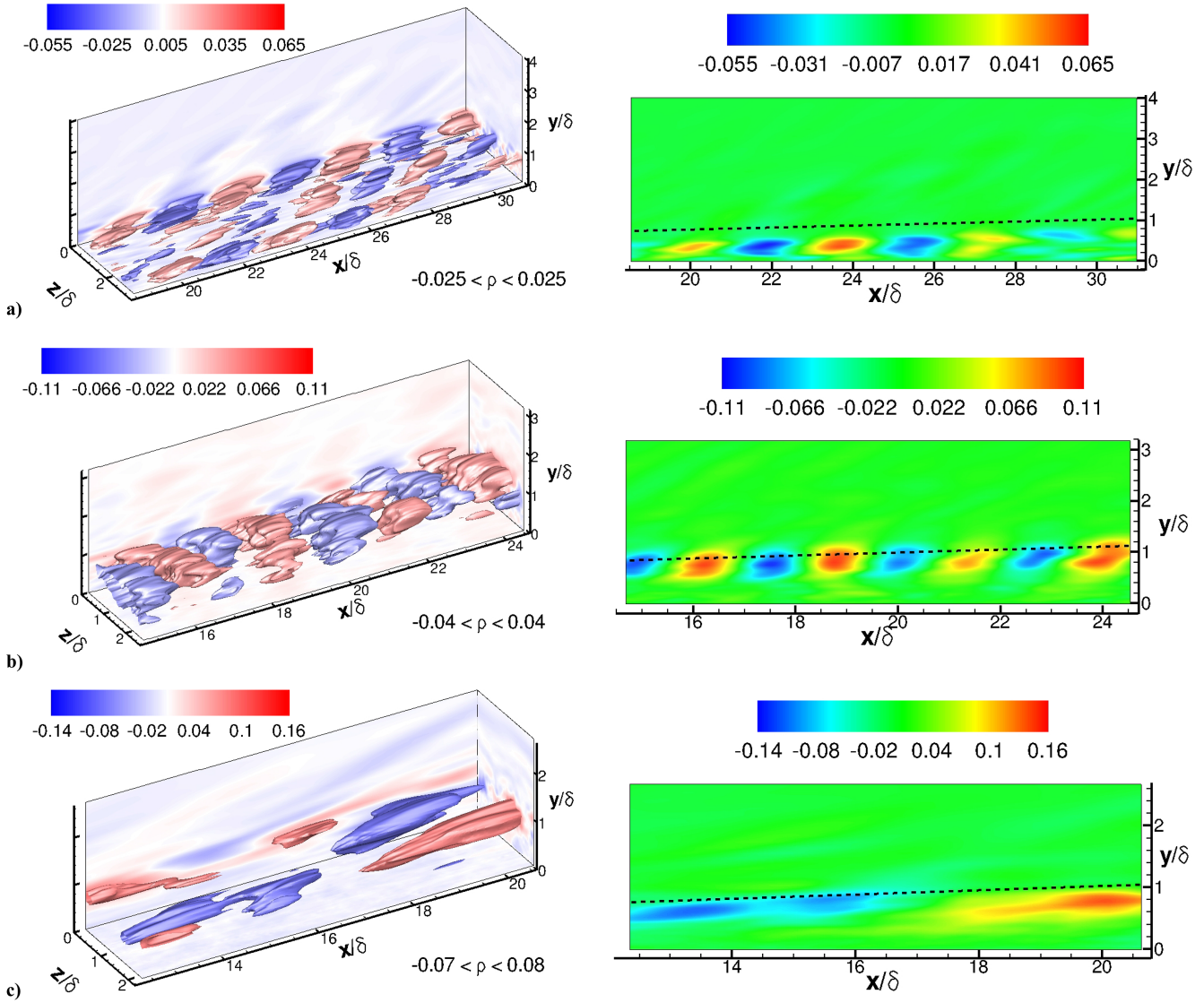

Fig. 15 Leading unsteady POD mode (mode 1) for density-based kernel. Instantaneous density isosurfaces flooded by density magnitude (left), and density isocontours for fixed z plane (right) for a) $M_\infty = 3.5$, b) $M_\infty = 7.87$, and c) $M_\infty = 13.64$.

Table 7 OPD_{rms} cumulative contribution (%) from leading 300 unsteady POD modes

M_∞ \ modes	25	50	100	150	200	300
3.5	72.46	86.14	96.06	98.93	99.80	100
7.87	82.57	91.27	97.58	99.37	99.89	100
13.64	82.60	92.06	97.88	99.47	99.91	100

density correlation length was investigated. Away from the wall, but inside the boundary layer, the correlation length is largest when the optical beam is tilted in the downstream direction [10,15]. Furthermore, the effect of the streamwise aperture on the aero-optical component of the beam jitter was investigated. For all Mach numbers, the aero-optical jitter decreases significantly with aperture size for $Ap_x < 4\delta$. In addition, a scaling relation for the aero-optical jitter was verified. The global jitter increases in amplitude for aperture sizes over 4δ.

Finally, for the chosen sampling interval, by using the POD, it was found that the leading 100 POD modes capture 90% of the density fluctuations for all Mach numbers. For the hypersonic Mach numbers, the leading POD modes represent density fluctuations directly underneath the boundary-layer edge. For Mach 8, the leading mode captures density fluctuations with spanwise coherence, while for Mach 14, the leading mode captures density fluctuations with streamwise coherence. The unsteady density fields were reconstructed from the POD modes, and the OPD_{rms} was computed. Convergence of the OPD_{rms} was observed for ≈70 POD modes for the $M_\infty = 3.5$ case and 50 POD modes for the hypersonic cases. This suggests that the leading 10–20% of the density-based POD modes are the main contributors to the OPD_{rms}. Investigating how the coherent structures contribute to the OPD may pave the way toward understanding the directional dependence of the density correlations and ultimately devising active flow control strategies geared toward a reduction of the OPD.

Overall, the present results also demonstrate that WMLES is a viable and computationally affordable alternative to DNS for computing the aero-optical distortion caused by high-speed compressible turbulent boundary layers. By evaluating the suitability of key underlying model relationships for high-Mach-number flows, such as the SRA and density correlation length, the present work makes a contribution to the extension of aero-optical models for hypersonic flows.

Acknowledgments

The support of the Laboratory Directed Research and Development program at Sandia National Laboratories is gratefully acknowledged. Sandia National Laboratories is a multimission laboratory managed and operated by National Technology & Engineering

Downloaded by University of Notre Dame on January 23, 2025 | http://arc.aiaa.org | DOI: 10.2514/1.J064115

Solutions of Sandia, LLC (NTESS), a wholly owned subsidiary of Honeywell International Inc., for the U.S. Department of Energy's National Nuclear Security Administration (DOE/NNSA) under contract DE-NA0003525. This written work is authored by an employee of NTESS. The employee, not NTESS, owns the right, title, and interest in and to the written work and is responsible for its contents. Any subjective views or opinions that might be expressed in the written work do not necessarily represent the views of the U.S. Government. The publisher acknowledges that the U.S. Government retains a nonexclusive, paid-up, irrevocable, worldwide license to publish or reproduce the published form of this written work or allow others to do so for U.S. Government purposes. The DOE will provide public access to results of federally sponsored research in accordance with the DOE Public Access Plan.

References

[1] Smits, A. J., and Dussauge, J.-P., *Turbulent Shear Layers in Supersonic Flow*, Springer Science & Business Media, Berlin, 2006. https://doi.org/10.1007/b137383

[2] Smith, R., Truman, C., and Masson, B., "Prediction of Optical Phase Degradation Using a Turbulent Transport Equation for the Variance of Index-of-Refraction Fluctuations," *28th Aerospace Sciences Meeting*, AIAA Paper 1990-0250, 1990. https://doi.org/10.2514/6.1990-250

[3] Miller, S. A., "Prediction of Turbulent Boundary-Layer Noise," *AIAA Journal*, Vol. 55, No. 5, 2017, pp. 1659–1672. https://doi.org/10.2514/1.J055087

[4] Wang, M., Mani, A., and Gordeyev, S., "Physics and Computation of Aero-Optics," *Annual Review of Fluid Mechanics*, Vol. 44, No. 1, 2012, pp. 299–321. https://doi.org/10.1146/annurev-fluid-120710-101152

[5] Gordeyev, S., Jumper, E., and Whiteley, M., *Aero-Optical Effects: Physics, Analysis and Mitigation*, Wiley Series in Pure and Applied Optics, Wiley, New York, 2023, https://books.google.com/books?id=hqujEAAAQBAJ.

[6] Liepmann, H., "Deflection and Diffusion of a Light Ray Passing Through a Boundary Layer," Santa Monica Div., Douglas Aircraft Company, Santa Monica, CA, 1952, https://books.google.com/books?id=C4 JMtAEACAAJ.

[7] Truman, C. R., and Lee, M. J., "Effects of Organized Turbulence Structures on the Phase Distortion in a Coherent Optical Beam Propagating Through a Turbulent Shear Flow," *Physics of Fluids A: Fluid Dynamics*, Vol. 2, No. 5, 1990, pp. 851–857. https://doi.org/10.1063/1.857633

[8] Truman, C., "The Influence of Turbulent Structure on Optical Phase Distortion Through Turbulent Shear Flows," *AIAA Annual Interceptor Technology Conference*, AIAA Paper 1992-2817, 1992. https://doi.org/10.2514/6.1992-2817

[9] Tromeur, E., Garnier, E., and Sagaut, P., "Large-Eddy Simulation of Aero-Optical Effects in a Spatially Developing Turbulent Boundary Layer," *Journal of Turbulence*, Vol. 7, Jan. 2006, p. N1. https://doi.org/10.1080/14685240500307389

[10] Cress, J., Gordeyev, S., Post, M., and Jumper, E., "Aero-Optical Measurements in a Turbulent, Subsonic Boundary Layer at Different Elevation Angles," *39th Plasmadynamics and Lasers Conference*, AIAA Paper 2008-4214, 2008. https://doi.org/10.2514/6.2008-4214

[11] Gordeyev, S., Jumper, E., and Hayden, T. E., "Aero-Optical Effects of Supersonic Boundary Layers," *AIAA Journal*, Vol. 50, No. 3, 2012, pp. 682–690. https://doi.org/10.2514/1.J051266

[12] Gordeyev, S., Smith, A. E., Cress, J. A., and Jumper, E. J., "Experimental Studies of Aero-Optical Properties of Subsonic Turbulent Boundary Layers," *Journal of Fluid Mechanics*, Vol. 740, Feb. 2014, pp. 214–253. https://doi.org/10.1017/jfm.2013.658

[13] Gordeyev, S., Cress, J. A., Smith, A., and Jumper, E. J., "Aero-Optical Measurements in a Subsonic, Turbulent Boundary Layer with Non-Adiabatic Walls," *Physics of Fluids*, Vol. 27, No. 4, 2015, Paper 045110. https://doi.org/10.1063/1.4919331

[14] Lynch, K. P., Miller, N. E., Guildenbecher, D. R., Butler, L., and Gordeyev, S., "Aero-Optical Measurements of a Mach 8 Boundary Layer," *AIAA Journal*, Vol. 61, No. 3, 2023, pp. 991–1001. https://doi.org/10.2514/1.j062363

[15] Wang, K., and Wang, M., "Aero-Optics of Subsonic Turbulent Boundary Layers," *Journal of Fluid Mechanics*, Vol. 696, April 2012, pp. 122–151. https://doi.org/10.1017/jfm.2012.11

[16] Zhang, C., Duan, L., and Choudhari, M. M., "Direct Numerical Simulation Database for Supersonic and Hypersonic Turbulent Boundary Layers," *AIAA Journal*, Vol. 56, No. 11, 2018, pp. 4297–4311. https://doi.org/10.2514/1.J057296

[17] Miller, N. E., Guildenbecher, D., and Lynch, K. P., "Aero-Optical Distortions of Turbulent Boundary Layers: DNS Up to Mach 8," *AIAA Aviation 2021 Forum*, AIAA Paper 2021-2832, 2021. https://doi.org/10.2514/6.2021-2832

[18] Miller, N. E., Lynch, K. P., Gordeyev, S., Guildenbecher, D. R., Duan, L., and Wagnild, R. M., "Aero-Optical Distortions of Turbulent Boundary Layers: Hypersonic DNS," *AIAA SciTech 2022 Forum*, AIAA Paper 2022-0056, 2022. https://doi.org/10.2514/6.2022-0056

[19] Castillo Gomez, P., Gross, A., Guildenbecher, D. R., Miller, N. E., and Lynch, K. P., "Wall-Modeled Large-Eddy Simulations of Mach 8 Turbulent Boundary Layer and Computation of Aero-Optical Distortions," *AIAA SciTech 2022 Forum*, AIAA Paper 2022-1674, 2022. https://doi.org/10.2514/6.2022-1674

[20] Castillo Gomez, P., Gross, A., Guildenbecher, D. R., Miller, N. E., and Lynch, K. P., "Wall-Modeled Large-Eddy Simulations of Turbulent Mach 3.5, 8, and 14 Boundary Layers-Effect of Mach Number on Aero-Optical Distortions," *AIAA Aviation 2022 Forum*, AIAA Paper 2022-3441, 2022. https://doi.org/10.2514/6.2022-3441

[21] Castillo, P., Gross, A., Miller, N. E., Lynch, K. P., and Guildenbecher, D. R., "Numerical Investigation of Wall-Cooling Effect on Aero-Optical Distortions for Hypersonic Boundary Layer," *AIAA Journal*, Vol. 61, No. 5, 2023, pp. 1911–1924. https://doi.org/10.2514/1.J062570

[22] Sutton, G. W., "Effect of Turbulent Fluctuations in an Optically Active Fluid Medium," *AIAA Journal*, Vol. 7, No. 9, 1969, pp. 1737–1743. https://doi.org/10.2514/3.5384

[23] Choi, H., and Moin, P., "Grid-Point Requirements for Large Eddy Simulation: Chapman's Estimates Revisited," *Physics of Fluids*, Vol. 24, No. 1, 2012, Paper 011702. https://doi.org/10.1063/1.3676783

[24] Yang, X., Sadique, J., Mittal, R., and Meneveau, C., "Integral Wall Model for Large Eddy Simulations of Wall-Bounded Turbulent Flows," *Physics of Fluids*, Vol. 27, No. 2, 2015, Paper 025112. https://doi.org/10.1063/1.4908072

[25] Catchirayer, M., Boussuge, J.-F., Sagaut, P., Montagnac, M., Papadogiannis, D., and Garnaud, X., "Extended Integral Wall-Model for Large-Eddy Simulations of Compressible Wall-Bounded Turbulent Flows," *Physics of Fluids*, Vol. 30, No. 6, 2018, Paper 065106. https://doi.org/10.1063/1.5030859

[26] Bocquet, S., Sagaut, P., and Jouhaud, J., "A Compressible Wall Model for Large-Eddy Simulation with Application to Prediction of Aerothermal Quantities," *Physics of Fluids*, Vol. 24, No. 6, 2012, Paper 065103. https://doi.org/10.1063/1.4729614

[27] Kawai, S., and Larsson, J., "Wall-Modeling in Large Eddy Simulation: Length Scales, Grid Resolution, and Accuracy," *Physics of Fluids*, Vol. 24, No. 1, 2012, Paper 015105. https://doi.org/10.1063/1.3678331

[28] Gordeyev, S., Jumper, E., and Hayden, T. E., "Aero-Optical Effects of Supersonic Boundary Layers," *AIAA Journal*, Vol. 50, No. 3, 2012, pp. 682–690. https://doi.org/10.2514/1.J051266

[29] Gordeyev, S., and Juliano, T. J., "Optical Characterization of Nozzle-Wall Mach-6 Boundary Layers," *54th AIAA Aerospace Sciences Meeting*, AIAA Paper 2016-1586, 2016. https://doi.org/10.2514/6.2016-1586

[30] Sutton, G. W., "Aero-Optical Foundations and Applications," *AIAA Journal*, Vol. 23, No. 10, 1985, pp. 1525–1537. https://doi.org/10.2514/3.9120

[31] Barone, M. F., Ling, J., Chowdhary, K., Davis, W., and Fike, J., "Machine Learning Models of Errors in Large Eddy Simulation Predictions of Surface Pressure Fluctuations," *47th AIAA Fluid Dynamics Conference*, AIAA Paper 2017-3979, 2017. https://doi.org/10.2514/6.2017-3979

[32] Gross, A., and Fasel, H., "High-Order WENO Schemes Based on the Roe Approximate Riemann Solver," *32nd AIAA Fluid Dynamics Conference and Exhibit*, AIAA Paper 2022-2735, 2002. https://doi.org/10.2514/6.2002-2735

[33] Gross, A., and Fasel, H., "High-Order Accurate Numerical Method for Complex Flows," *AIAA Journal*, Vol. 46, No. 1, 2008, pp. 204–214. https://doi.org/10.2514/1.22742

[34] Nicoud, F., and Ducros, F., "Subgrid-Scale Stress Modelling Based on the Square of the Velocity Gradient Tensor," *Flow, Turbulence and*

Downloaded by University of Notre Dame on January 23, 2025 | http://arc.aiaa.org | DOI: 10.2514/1.J064115

Combustion, Vol. 62, No. 3, 1999, pp. 183–200.
https://doi.org/10.1023/A:1009995426001

[35] Stolz, S., and Adams, N. A., "Large-Eddy Simulation of High-Reynolds-Number Supersonic Boundary Layers Using the Approximate Deconvolution Model and a Rescaling and Recycling Technique," *Physics of Fluids*, Vol. 15, No. 8, 2003, pp. 2398–2412.
https://doi.org/10.1063/1.1588637

[36] Larsson, J., Kawai, S., Bodart, J., and Bermejo-Moreno, I., "Large Eddy Simulation with Modeled Wall-Stress: Recent Progress and Future Directions," *Mechanical Engineering Reviews*, Vol. 3, No. 1, 2016, pp. 15–00418.
https://doi.org/10.1299/mer.15-00418

[37] Keyes, F., "A Summary of Viscosity and Heat-Conduction Data for He, A, H_2, O_2, N_2, CO, CO_2, H_2O, and Air," *Transactions of the American Society of Mechanical Engineers*, Vol. 73, No. 5, 1951, pp. 589–595.
https://doi.org/10.1115/1.4016339

[38] Gladstone, J. H., and Dale, T. P., "XIV. Researches on the Refraction, Dispersion, and Sensitiveness of Liquids," *Philosophical Transactions of the Royal Society of London*, Vol. 153, Jan. 1863, pp. 317–343.
https://doi.org/10.1098/rstl.1863.0014

[39] Peck, E. R., and Khanna, B. N., "Dispersion of Nitrogen," *Journal of the Optical Society of America*, Vol. 56, No. 8, 1966, pp. 1059–1063.
https://doi.org/10.1364/JOSA.56.001059

[40] Clergent, Y., Durou, C., and Laurens, M., "Refractive Index Variations for Argon, Nitrogen, and Carbon Dioxide at $\lambda = 632.8$ nm (He-Ne laser light) in the Range 288.15 K $\leq$ T $\leq$ 323.15 K, 0 < p < 110 kPa," *Journal of Chemical & Engineering Data*, Vol. 44, No. 2, 1999, pp. 197–199.
https://doi.org/10.1021/je980133o

[41] Kemnetz, M. R., and Gordeyev, S., "Analysis of Aero-Optical Jitter in Convective Turbulent Flows Using Stitching Method," *AIAA Journal*, Vol. 60, No. 1, 2022, pp. 14–30.
https://doi.org/10.2514/1.J060756

[42] Kemnetz, M. R., and Gordeyev, S., "Optical Investigation of Large-Scale Boundary-Layer Structures," *54th AIAA Aerospace Sciences Meeting*, AIAA Paper 2016-1460, 2016.
https://doi.org/10.2514/6.2016-1460

[43] Lumley, J. L., "The Structure of Inhomogeneous Turbulent Flows," *Atmospheric Turbulence and Radio Wave Propagation*, Nauka, Moscow, Russia, 1967, pp. 166–178, https://cir.nii.ac.jp/crid/1574231878454277171.

[44] Sirovich, L., "Turbulence and the Dynamics of Coherent Structures, Parts I, II and III," *Quarterly of Applied Mathematics*, Vol. 45, 1987, pp. 561–590, https://www.jstor.org/stable/43637457.

[45] Taira, K., Brunton, S. L., Dawson, S. T., Rowley, C. W., Colonius, T., McKeon, B. J., Schmidt, O. T., Gordeyev, S., Theofilis, V., and Ukeiley, L. S., "Modal Analysis of Fluid Flows: An Overview," *AIAA Journal*, Vol. 55, No. 12, 2017, pp. 4013–4041.
https://doi.org/10.2514/1.J056060

[46] Rowley, C. W., Colonius, T., and Murray, R. M., "Model Reduction for Compressible Flows Using POD and Galerkin Projection," *Physica D: Nonlinear Phenomena*, Vol. 189, Nos. 1–2, 2004, pp. 115–129.
https://doi.org/10.1016/j.physd.2003.03.001

[47] Walz, A., *Boundary Layers of Flow and Temperature*, MIT Press, Cambridge, MA, 1969, https://books.google.com/books?id=nUPLuQEACAAJ.

[48] Duan, L., Beekman, I., and Martin, M., "Direct Numerical Simulation of Hypersonic Turbulent Boundary Layers: Part 2. Effect of Wall Temperature," *Journal of Fluid Mechanics*, Vol. 655, July 2010, pp. 419–445.
https://doi.org/10.1017/S0022112010000959

[49] Wyckham, C. M., and Smits, A. J., "Aero-Optic Distortion in Transonic and Hypersonic Turbulent Boundary Layers," *AIAA Journal*, Vol. 47, No. 9, 2009, pp. 2158–2168.
https://doi.org/10.2514/1.41453

[50] Zhang, C., and Duan, L., "Acoustic Radiation from a Mach 14 Turbulent Boundary Layer," *54th AIAA Aerospace Sciences Meeting*, AIAA Paper 2016-0048, 2016.
https://doi.org/10.2514/6.2016-0048

[51] Jumper, E. J., and Gordeyev, S., "Physics and Measurement of Aero-Optical Effects: Past and Present," *Annual Review of Fluid Mechanics*, Vol. 49, Jan. 2017, pp. 419–441.
https://doi.org/10.1146/annurev-fluid-010816-060315

[52] Duan, L., Choudhari, M. M., and Wu, M., "Numerical Study of Acoustic Radiation Due to a Supersonic Turbulent Boundary Layer," *Journal of Fluid Mechanics*, Vol. 746, May 2014, pp. 165–192.
https://doi.org/10.1017/jfm.2014.116

[53] Duan, L., Choudhari, M. M., and Zhang, C., "Pressure Fluctuations Induced by a Hypersonic Turbulent Boundary Layer," *Journal of Fluid Mechanics*, Vol. 804, Oct. 2016, pp. 578–607.
https://doi.org/10.1017/jfm.2016.548

[54] Zhang, C., Duan, L., and Choudhari, M. M., "Effect of Wall Cooling on Boundary-Layer-Induced Pressure Fluctuations at Mach 6," *Journal of Fluid Mechanics*, Vol. 822, July 2017, pp. 5–30.
https://doi.org/10.1017/jfm.2017.212

[55] Morkovin, M. V., "Effects of Compressibility on Turbulent Flows," *Mécanique de la Turbulence*, Vol. 367, No. 380, 1962, p. 26.

[56] Lele, S. K., "Compressibility Effects on Turbulence," *Annual Review of Fluid Mechanics*, Vol. 26, No. 1, 1994, pp. 211–254.
https://doi.org/10.1146/annurev.fl.26.010194.001235

[57] Guarini, S. E., Moser, R. D., Shariff, K., and Wray, A., "Direct Numerical Simulation of a Supersonic Turbulent Boundary Layer at Mach 2.5," *Journal of Fluid Mechanics*, Vol. 414, July 2000, pp. 1–33.
https://doi.org/10.1017/S0022112000008466

[58] Hadjadj, A., Ben-Nasr, O., Shadloo, M., and Chaudhuri, A., "Effect of Wall Temperature in Supersonic Turbulent Boundary Layers: A Numerical Study," *International Journal of Heat and Mass Transfer*, Vol. 81, Feb. 2015, pp. 426–438.
https://doi.org/10.1016/j.ijheatmasstransfer.2014.10.025

[59] Maeder, T., Adams, N. A., and Kleiser, L., "Direct Simulation of Turbulent Supersonic Boundary Layers by an Extended Temporal Approach," *Journal of Fluid Mechanics*, Vol. 429, Feb. 2001, pp. 187–216.
https://doi.org/10.1017/S0022112000002718

[60] Gaviglio, J., "Reynolds Analogies and Experimental Study of Heat Transfer in the Supersonic Boundary Layer," *International Journal of Heat and Mass Transfer*, Vol. 30, No. 5, 1987, pp. 911–926.
https://doi.org/10.1016/0017-9310(87)90010-X

[61] Rubesin, M. W., "Extra Compressibility Terms for Favre-Averaged Two-Equation Models of Inhomogeneous Turbulent Flows," National Aeronautics and Space Administration (NASA), NAS 1.26:177556, Washington, D.C., 1990, https://nla.gov.au/nla.cat-vn4178292.

[62] Huang, P., Coleman, G. N., and Bradshaw, P., "Compressible Turbulent Channel Flows: DNS Results and Modelling," *Journal of Fluid Mechanics*, Vol. 305, Dec. 1995, pp. 185–218.
https://doi.org/10.1017/S0022112095004599

[63] Brun, C., Petrovan Boiarciuc, M., Haberkorn, M., and Comte, P., "Large Eddy Simulation of Compressible Channel Flow: Arguments in Favour of Universality of Compressible Turbulent Wall Bounded Flows," *Theoretical and Computational Fluid Dynamics*, Vol. 22, May 2008, pp. 189–212.
https://doi.org/10.1007/s00162-007-0073-y

[64] Zhang, Y.-S., Bi, W.-T., Hussain, F., and She, Z.-S., "A Generalized Reynolds Analogy for Compressible Wall-Bounded Turbulent Flows," *Journal of Fluid Mechanics*, Vol. 739, Jan. 2014, pp. 392–420.
https://doi.org/10.1017/jfm.2013.620

[65] Robinson, S. K., "Coherent Motions in the Turbulent Boundary Layer," *Annual Review of Fluid Mechanics*, Vol. 23, No. 1, 1991, pp. 601–639.
https://doi.org/10.1146/annurev.fl.23.010191.003125

F. Grasso
Associate Editor

Downloaded by University of Notre Dame on January 23, 2025 | http://arc.aiaa.org | DOI: 10.2514/1.J064115